Normal impact force of Rayleigh jets

Benjamin R. Mitchell ●,[1,*] Joseph C. Klewicki,[2] Yannis P. Korkolis ●,[3] and Brad L. Kinsey[1]

[1]*Department of Mechanical Engineering, University of New Hampshire, Durham,*
New Hampshire 03824, USA
[2]*Department of Mechanical Engineering, University of Melbourne, Victoria 3010, Australia*
[3]*Department of Integrated Systems Engineering, The Ohio State University, Columbus, Ohio 43210, USA*

The surface-normal impingement of a liquid jet emanating from a nozzle is of use in numerous technological applications (e.g., surface cleaning, waterjet cutting, and needle-free injection). Upon impact, the (Rayleigh) jet is characterized as either a steady-state (time-invariant) jet, a wavy jet, or a droplet train. The present study experimentally investigates the force imparted by these three distinctly different processes for identical nozzle flow conditions (i.e., velocity and jet diameter). Force models are developed based on Rayleigh jet theory, and they are shown to compare well with the measurements. The force induced by the wavy jet is sinusoidal, oscillating about the steady-state force, while the droplet train force is discrete with periods of zero induced force. Due to conservation of momentum, the peak force experienced by the droplet train is significantly higher than that of the steady stream. This identifies the droplet train as the dominant process to obtain higher peak forces than the continuous stream counterparts during impact with a surface. This can then be used as a means to increase the performance of applications such as waterjet cutting and surface cleaning.

I. INTRODUCTION

The impact of a liquid jet is used in numerous applications, e.g., surface cleaning [1], cooling [2,3], coating and ink-jet printing [4], surgical applications [5,6], and medicine delivery [7]. In most of these applications, a liquid is accelerated through a circular orifice that initially forms either a continuous, axisymmetric, cylindrical (Rayleigh) jet or is emitted as a disorganized mass of liquid droplets by a process known as atomization [8]. Many of the applications listed above utilize the former process, where an initially continuous stream of liquid travels a certain distance from the orifice until colliding with a surface. The purposes of surface impingement vary depending on the application. In coating flows or ink-jet printing, for example, it is often desirable to efficiently deposit the liquid onto the surface while minimizing splash [9,10] (i.e., in order to enhance print quality). In surface cleaning or waterjet cutting, it is advantageous to maximize the stress imparted onto the surface (i.e., to remove dirt or to penetrate the surface for effective material removal). Upon impact with the surface, however, the liquid in the emanating jet can exhibit two distinctly different states: (i) the liquid remains intact as a continuous, axisymmetric jet, depicted in Figs. 1(a) and 1(b); or (ii) the liquid jet fragments, downstream of the orifice, into a train of discrete droplets due to a surface tension induced instability [11], shown in Fig. 1(c). Regardless of the intended application, the characteristics of the impact (i.e., splash, induced force, etc.) will change depending on whether the liquid is in a droplet state upon impact or remains as a continuous jet. Here, it is recognized that
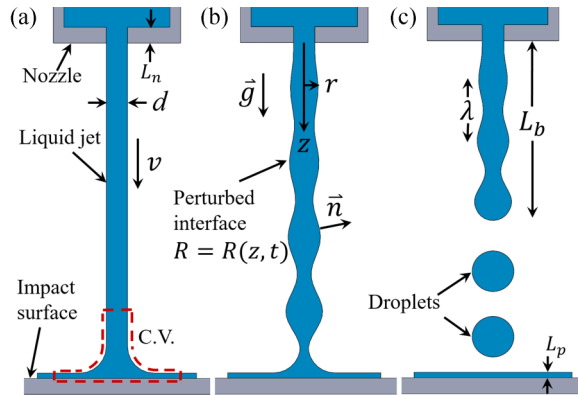
---

*bre36@wildcats.unh.edu

FIG. 1. Schematic of the normal impingement of Rayleigh jets: (a) steady-state jet, (b) wavy jet, and (c) droplet train.

a Rayleigh jet constitutes any of the Fig. 1 depictions, as the only differences between these jets are their perturbation amplitudes and whether these amplitudes are large enough to permit droplet formation. The state of the liquid arriving normal to the impingement surface is then governed by the perturbation amplitude and the nozzle to plate distance, as described in detail in Secs. II and III.

The droplet formation process from a continuous jet has received considerable attention since the pioneering work of Lord Rayleigh [11–13]. Similarly, the impact of a single droplet onto a flat solid surface has received a wealth of scientific interest, with particular attention paid to the underlying splashing mechanisms [14,15]. A less prevalent research topic is the associated impact of continuous jets, and droplet trains onto flat solid surfaces, and especially the induced normal force. This area remains largely unexplored; however, knowledge of the force induced by Rayleigh jets is of practical use in industrial applications and is of broad scientific interest. In fact, as a unique example, archer fish (*Toxotes jaculatrix*) attack their above-surface prey with precisely aimed waterjets [16].

In this study, the similarities and differences of the normal impingement of a steady-state jet, a wavy jet, and a droplet train onto a solid surface are investigated through force measurements and high-speed photography. Our aim is to quantify the force imparted by these distinctly different scenarios for identical nozzle flow conditions (i.e., velocity and jet diameter). In this way, the momentum exiting the nozzle is identical for each condition, allowing for direct comparison. A quantitative understanding in the applied force of Rayleigh jets allows applications to be designed with sufficient foresight, and aids in determining whether the use of droplets is appropriate and beneficial.

This paper begins with the regimes associated with the "breakup" of liquid jets in Sec. II, followed by a description of the droplet formation process in Sec. III. That section also characterizes the jet free-surface, which is used to formulate model equations for the force induced by continuous jets in Sec. IV. Section V elucidates the force imparted by a single droplet, which is used in series to formulate a model equation for the force induced by a droplet train. These force models are then experimentally tested. In Sec. VI the experimental setup and data processing methods are introduced. This is followed by results and discussion in Sec. VII, and finally we end with conclusions in Sec. VIII.

II. CLASSIFICATION OF JET REGIMES

Liquid issuing from a circular nozzle has several outcomes. If the flow rate exiting the nozzle is relatively small, and there exists a quasistatic balance between the liquid inertial/gravitational force and the surface tension force, then the liquid simply drips [17] (i.e., a leaking faucet). As the flow rate increases, the liquid takes the form of a cylindrical "Rayleigh" jet, where the jet appears smooth

and unperturbed close to the nozzle. The onset between the dripping regime and the Rayleigh regime occurs when the Weber number (ratio of inertial to surface tension force) exceeds a critical threshold, described by

$$\mathrm{We} = \frac{\rho d_0 v_0^2}{\sigma} > 8, \tag{1}$$

where ρ is the liquid density, d_0 is the jet diameter, v_0 is the jet velocity relative to the nozzle, and σ is the surface tension [18–20]. A formal description of the transition from dripping to jetting can be found in Ref. [21]. Once in the Rayleigh regime, the liquid exiting the nozzle is initially columnar; however, at a certain distance downstream, wavy disturbances about the free surface become discernible. These disturbances grow progressively in amplitude downstream until the wave amplitude becomes approximately equal to the jet radius. This is where droplet formation occurs [22]. The distance between the nozzle and the point of droplet formation is defined as the breakup length L_b [see Fig. 1(c)], and is linearly proportional to the jet velocity. More specifically, the normalized breakup length scales with the square root of the jet's Weber number (i.e., $L_b/d_0 \propto \sqrt{\mathrm{We}}$) [13,23–27]. This relation, however, is valid only for a certain range of Weber numbers. As the jet velocity increases, the surrounding fluid into which the jet is immersed (typically air) begins to alter the Rayleigh regime dynamics. Aerodynamic drag causes droplet formation to occur earlier, shortening the breakup length. The breakup length begins to decrease nonlinearly with jet velocity, and the jet enters the first wind-induced regime [13]. This occurs when the aerodynamic force is about 10% of the surface tension force [28]. A further increase in the jet velocity allows the surrounding fluid to induce significant shearing stress onto the jet. This causes droplets to be stripped off the surface rather than being pinched off in segments at the fore of the jet [22]. The jet then enters successive wind-induced and atomization regimes.

The topic of this paper focuses solely on Rayleigh jets. A comprehensive review of the subsequent regimes can be found in Refs. [13,19,23,29]. The upper bound separating the Rayleigh regime from the first wind-induced regime is described by

$$\mathrm{We} < 0.4 \frac{\rho}{\rho_{\mathrm{gas}}}, \tag{2}$$

where ρ_{gas} is the density of the ambient gas [19,20,29]. For the experiments reported in this paper, which are conducted in standard atmosphere, the critical upper bound for velocity is 3.8 m/s. Note that Eq. (2) predicts that the Rayleigh regime can be extended to higher jet velocities if the surrounding atmospheric pressure is reduced. This widening of the Rayleigh regime has been experimentally verified by Fenn and Middleman in a subatmospheric pressure environment [30].

III. DROPLET FORMATION FROM RAYLEIGH JETS

As previously mentioned, a Rayleigh jet is characterized by an initially continuous, unbroken stream of liquid emanating from a nozzle that with downstream evolution may break apart into discrete droplets due to surface tension-induced instabilities. If a flat solid surface is positioned normal to the jet, before the region where wavy disturbances become noticeable, then the liquid is diverted radially along the surface, as depicted in Fig. 1(a). If the axial disturbances have sufficiently large amplitudes, droplet formation will occur closer to the nozzle, and a flat solid surface positioned past the breakup length will experience a series of droplet impacts, like that shown in Fig. 1(c). Figure 1(a) is a highly idealized scenario as disturbances are likely to occur and grow in amplitude almost immediately after the nozzle exit. There exists an intermediate scenario between the steady columnar jet impact and the droplet train impact. In this scenario, the solid surface will experience a series of continuous wave impacts, like that depicted in Fig. 1(b). If viscous effects of the impinging jet can be neglected, and the Weber number satisfies Eqs. (1) and (2), then predicting the state in which the liquid arrives at the surface is accomplished through Rayleigh jet theory.

A. Plateau's reasoning

The first attempt to characterize the droplet formation process was done by Plateau in 1873. At this time, it was known that liquids possess a binding force at their free surface, i.e., surface tension (N/m in S.I. units) or surface energy (J/m^2). In terms of total surface energy, a given volume of liquid can exhibit different surface areas (depending on its shape), which correspond to different surface energies. Based on the principle of minimum potential energy, Plateau reasoned that an axisymmetric, wavy liquid column of radius

$$R(z) = R_0 + ae^{ikz}, \tag{3}$$

where R_0 is the mean column radius (i.e., $R_0 = d_0/2$), $a \ll R_0$ is the wave amplitude, $i = \sqrt{-1}$, and k is the wave number, exhibits a smaller surface area (and thus a lower potential energy) than that of a straight cylindrical column of equal volume, if the wavelength $\lambda = 2\pi/k$ is larger than the column's circumference [31]. This principle of energy minimization essentially derives from the second law of thermodynamics, and permits the unstable wavy liquid column to discretize into droplets whose combined surface area is less than that of the original column. Disturbances or waves that are nonaxisymmetric (i.e., azimuthal modulations) are stable [13,32,33]. For axisymmetric jets, only wave numbers in the range $0 < kR_0 < 1$ are unstable and lead to droplet formation. Although a critical finding, this range does not identify which wave(s) are most dominant or how rapidly different waves grow in amplitude.

B. Rayleigh's local analysis

Using the equations of motion, Rayleigh determined the wave number associated with the most rapid wave amplitude growth. He considered the evolution of small axisymmetric perturbations about the free surface of a quiescent, inviscid, infinitely long liquid cylinder, with radius R_0, density ρ, and surface tension σ, in the absence of gravity. These small perturbations (i.e., waves) allow linearization of the momentum equations, which, with the continuity equation and appropriate boundary conditions, yield their temporal growth rates, ω. In Rayleigh's analysis, the free surface takes the form of a perturbed sinusoidal column about the axial direction z, as described by

$$R(z,t) = R_0 + ae^{\omega t + ikz}, \tag{4}$$

where ω and k are the previously defined growth rate and wave number, respectively. Negative values of ω lead to wave stabilization, while positive values lead to wave steepening and imminent droplet formation. The prominent result of Rayleigh's analysis is a dispersion relation. This describes the dependence of the wave growth rate on wave number, and it is given by

$$\frac{\rho\omega^2 R_0^3}{\sigma} = kR_0 \frac{I_1(kR_0)}{I_0(kR_0)}\left(1 - k^2 R_0^2\right), \tag{5}$$

where I_ν is the modified Bessel function of the first kind. This relation is plotted in Fig. 2. The wave number of the fastest growing wave is $kR_0 = 0.697$. Other waves can, however, lead to the discretization of the column if their initial amplitudes are sufficiently large. It should be noted that this linearized wave model accurately describes the early stages of jet segmentation. The actual pinch-off of the droplet can only be described by nonlinear theories [34]. The infinite column is allowed to travel in space with some arbitrary velocity, but waves do not propagate upstream or downstream with respect to the bulk flow. In this regard, Rayleigh's analysis can be seen as a local theory, as every wave along the column is identical to the wave upstream or downstream of it. Therefore, one only needs a portion of the column $\lambda = 2\pi/k$ to completely describe its characteristics. This is obviously not the case for finite liquid jets issuing from nozzles, as waves progressively grow in amplitude along the axial direction.
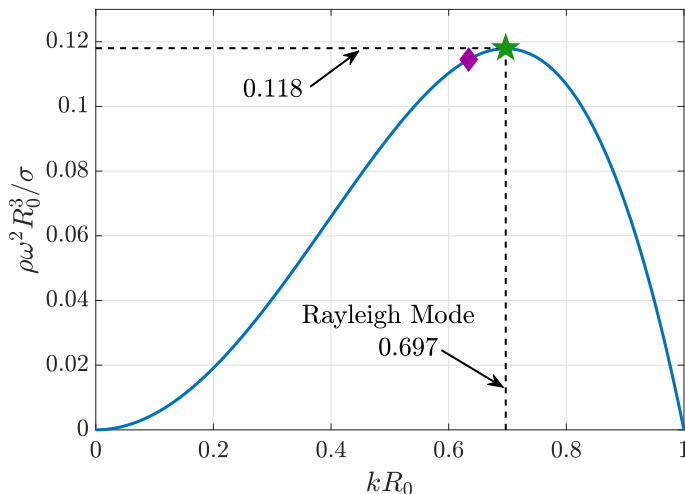
FIG. 2. Rayleigh's dispersion relation identifying the dependence of wave growth rate ω on the normalized wave number kR_0. The fastest growing wave (Rayleigh mode) occurs for $kR_0 = 0.697$, labeled with a green star. The wave number at impact for our experiments is $kR_0 = 0.634$, and it is represented with a purple diamond.

C. Spatial analysis

Rayleigh's analysis can be extended to liquid jets issuing from nozzles in a commonly used spatial theory [35–38]. In this theory, waves grow in amplitude along the z direction, rather than in time. This fixes the breakup length for steady-state jets, and is the case for our experiments. This spatial description of the free surface is the intuitive choice for the laboratory reference frame; however, there are certain assumptions that must be made. Namely, the temporal characteristics propagate downstream in the axial direction with the same velocity of the jet $\bar{v}$. This requires one to define a new parameter: the spatial wave frequency, K, which connects to the temporal wave number as $K = k = 2\pi/(vT)$, where T is the period of temporal oscillation. The period is related to the frequency by $T = 1/f$, and the wavelength is then $\lambda = vT$. The temporal wave growth rate is related to the spatial growth rate β through $\beta = \omega/v$. With these considerations, the free surface of the jet takes the form

$$R(z, t) = R_0 + ae^{\beta z}\cos(Kz - 2\pi ft + \phi), \qquad (6)$$

where ϕ is the phase of the wave, which is arbitrary and depends on the time in which the analysis starts. The nozzle location is at $z = 0$, with positive z being the direction toward the impact surface (see Fig. 1). Equation (6) indicates that the waves oscillate both in time and in space. When traveling with a wave at velocity $\bar{v}$, an observer will simply see wave amplitude growth and then droplet formation. If it is at a fixed z location, then the observer sees waves of equal amplitude (or droplets) pass by at a rate given by f. If one droplet is produced per wavelength, then by mass conservation the diameter of the droplet D is given by $D = (1.5\lambda d^2)^{1/3}$. For the Rayleigh mode $\lambda = \pi d/0.697$, the droplet diameter is nearly twice the jet diameter (i.e., $D = 1.89d$). Despite this, most studies [20,39–41] show a range of droplet diameters within two distinct subsets, namely primary droplets and satellite droplets, which are significantly smaller than primary drops. Rayleigh theory does not predict satellite droplet formation, as this theory is strictly linear and only considers small perturbations from equilibrium. The formation of satellite droplets can be anticipated from nonlinear theories where breakup profiles are self-similar [42]. Satellite drops form in between primary droplets at the breakup length L_b. Although the breakup length is typically considered constant, it may vary slightly from each droplet pinch-off. It has been shown that the breakup length is well represented by a Gaussian distribution, with Gaussian width proportional to the jet

velocity [23,24,29]. This natural breakup length may be artificially shortened through wave-number stimulation.

D. Stimulated droplet formation

A number of methods have been used to stimulate jets in order for droplets to form closer to the nozzle. This may be done through elliptically shaped nozzles [25,32,33], piezoelectric vibration [43], reservoir pressure oscillation [27], or simply by exploiting any periodic disturbance in the vicinity of the jet, which may be an audio speaker placed next to the nozzle exit [44]. Depending on the stimulation frequency f, these methods generate a large initial wave amplitude a that is specific to the excited wavelength λ. This allows certain wave numbers to become the dominant wave (instead of the Rayleigh wave) and thus the wave responsible for droplet formation. A range of wave numbers may be stimulated, but only those in the range $0 < kR_0 < 1$ permit droplet formation. Due to the increased amplitude, artificial stimulation enables droplets to form sooner and thus closer to the nozzle. Other means may be used to shorten the breakup length, such as the choice of nozzle geometry.

E. Effects of nozzle geometry

The velocity profile exiting the nozzle is important, especially if precise control of the breakup length is required. Nozzles with short aspect ratios ($L_n/d_n < 1$), where L_n is the nozzle length (see Fig. 1) and d_n is the nozzle diameter, are more stable and produce more consistent droplets than nozzles with long aspect ratios [29]. Pipe flow turbulence associated with long nozzle aspect ratios leads to moderate shortening of the breakup length [45]. Although the nozzle aspect ratio affects the breakup length, it also influences the diameter of the jet itself, as the jet diameter d_0 may not necessarily equal the nozzle diameter d_n. The study by Gavis and Modan shows that the contraction ratio $\chi = d_0/d_n$ is dependent on the jet Reynolds number, defined as $\mathrm{Re}_n = \rho d_n v_0/\mu$, where μ is the fluid viscosity. Contraction of the jet (i.e., $\chi < 1$) occurs for $\mathrm{Re} > 16$, while expansion (i.e., $\chi > 1$) occurs for $\mathrm{Re} < 16$ [46]. For example, $\mathrm{Re} = 100$ liquid flow through a nozzle of aspect ratio $L_n/d_n = 0.5$ exhibits about 7% contraction. The velocity profile relaxation is completed after liquid from the nozzle travels approximately one nozzle length $O(L_n)$; after this, the jet diameter remains unchanged [46]. This indicates that for short nozzle aspect ratios, the jet diameter d_0 may be assessed close to the nozzle.

F. Other analyses

Rayleigh's analysis shows that the droplet formation process is governed purely by the growth of capillary waves whose wavelength is a function of the liquid properties and jet diameter only. It is worth noting that Rayleigh's theory has been extended to other analyses conducted by Weber [47], Yuen [48], Sterling and Schleicher [28], and Leib and Golstein [35], which take into account the fluid viscosity, velocity, nonlinearity, and effects of ambient air. The effects of viscosity tend to decrease the growth rate and increase the dominant wavelength [22]. For the purposes of our analysis, the spatial form of Rayleigh's theory is instructive as it elucidates the droplet formation mechanisms and accurately represents the jet free-surface, which can be used to yield accurate models for the induced force of real jets.

IV. FORCE INDUCED BY CONTINUOUS JETS

A. Steady-state jets

The steady-state normal impingement force of a continuous unperturbed jet, like that depicted in Fig. 1(a), can be determined through control volume analysis. The volume considered is the curved area at the base of the jet in contact with the surface revolved about the z axis. It is assumed that the incoming flow is uniform with velocity $\vec{v}$, and the outward deflected radial flow travels purely in

the r direction. The jet Reynolds number is assumed to be sufficiently high such that viscous effects are negligible. With these considerations, the integral momentum equation may be applied to the control volume to yield the jet impact force

$$F = \frac{\pi}{4} \rho v_0^2 d_0^2. \tag{7}$$

The parameters ρ, v_0, and d_0 provide an inertial set of normalizing parameters, such that the nondimensional form of Eq. (7) is $\hat{F} = F/\rho v_0^2 d_0^2 = \pi/4$. Equation (7) is effectively a statement of momentum conservation, as the plate simply diverts the jet momentum from the axial to the radial direction.

If gravitational effects are considered, then the jet velocity increases with increasing z and the jet radius contracts as a consequence of mass conservation. The velocity in the axial direction at the moment of impact is defined as v, while v_0 is the nozzle exit velocity. If the Weber number is sufficiently high such that surface tension can be neglected, and air-induced drag is considered negligible, then the jet velocity at impact takes the form

$$\frac{v(z)}{v_0} = \left(1 + \frac{1}{\mathrm{Fr}} \frac{z}{R_0} \right)^{1/2}, \tag{8}$$

where the Froude number $\mathrm{Fr} = v_0^2/(d_0 g)$ represents the ratio of fluid inertial force to gravitational force. The radius is similarly given by

$$\frac{R(z)}{R_0} = \left(1 + \frac{1}{\mathrm{Fr}} \frac{z}{R_0} \right)^{-1/4}. \tag{9}$$

The derivation for velocity and radius evolution can be found in Appendix. To consider the effects of gravity on jet impingement force, Eqs. (8) and (9) are substituted into the normalized form of Eq. (7) to yield

$$\hat{F}_a(z) = \frac{\pi}{4} \left(1 + \frac{1}{\mathrm{Fr}} \frac{z}{R_0} \right)^{1/2}, \tag{10}$$

where the subscript a refers to the scenario depicted in Fig. 1(a), as this jet exists in a gravitational field. If gravitational effects are weak (i.e., $\mathrm{Fr} \rightarrow \infty$), then Eq. (10) reduces to the normalized form of Eq. (7). Equation (10) is perhaps a more realistic model as many industrial jets are influenced by gravity, however this equation does not account for free-surface perturbations.

B. Wavy jets

To determine the effect of waves on the jet impingement force, Rayleigh's description of the free surface given by Eq. (6) is employed. This implies that the radius of the impinging jet is time-periodic at any given fixed plate location, defined as $z = Z$. A control volume analysis is used, similar to the steady-state jet, but now with a spatially varying control volume. The control volume is now the area of the jet bounded by the (time-dependent) free surface and the base in contact with the plate revolved about the z axis. The flow is assumed uniform at the top boundary of the control volume and at the exit. Rayleigh's theory indicates that there exist axial and radial velocities associated with the capillary pinching of the jet. These velocities are, however, negligible compared to the bulk velocity $\bar{v}$. Therefore, at the top boundary, there exists uniform flow of velocity $\bar{v}$, with a time-varying cross-sectional area. It is assumed that the top boundary is very close to the plate, permitting evaluation at the plate location, $z = Z$. Applying the integral momentum equation to this control volume yields

$$\hat{F}_{\mathrm{wavy}}(z, t) = \frac{\pi}{4} [1 + 2\epsilon e^{\beta z} \cos(\zeta - 2\pi f t)], \tag{11}$$

where $\zeta = Kz + \phi$ is a parameter to shift the phase as required, and $\epsilon = a/R_0 \ll 1$ is the normalized initial wave amplitude. As anticipated, Eq. (11) is oscillatory in time and fluctuates about the steady-state force given by Eq. (7). Note that the amplitude of oscillation increases exponentially in the z direction. If the impact surface exceeds the breakup length (i.e., $Z > L_b$), then this model would obviously not be applicable as droplets would impact the surface instead of a wavy jet. Due to the linearized small perturbation theory incorporated into Eq. (11), this model is anticipated to only work for small wave amplitudes. Although Eq. (11) exhibits z dependence, gravitational effects are not included.

In a similar way to the steady-state jet, gravity will increase the jet velocity according to Eq. (8), and reduce the time-invariant radius according to Eq. (9). With these considerations, the gravitational dependent form of Eq. (11) becomes

$$\hat{F}_b(z,t) = \frac{\pi}{4}(1 + 2\epsilon e^{\beta z} \cos(\zeta - 2\pi f t))\left(1 + \frac{1}{\mathrm{Fr}}\frac{z}{R_0}\right)^{1/2}, \tag{12}$$

where the subscript b refers to the scenario depicted in Fig. 1(b). If gravitational effects are deemed negligible (i.e., $\mathrm{Fr} \to \infty$), then Eq. (12) reduces to Eq. (11). In addition, if the jet does not exhibit wavy oscillations about the free surface (i.e., $\epsilon e^{\beta z} \to 0$), then Eq. (12) reduces to Eq. (10). It must be noted that, due to gravity, waves are stretched along the axial direction. Therefore, the wave number decreases with z, and thus waves take on a range of growth rates before impact. A comprehensive report on the consequences of jet elongation was presented by Frankel and Weihs [49]. The normalized wave number incorporating gravitational dependence is given by

$$k(z) = \frac{2\pi f}{v_0}\left(1 + \frac{1}{\mathrm{Fr}}\frac{z}{R_0}\right)^{-1/2}. \tag{13}$$

Although the waves change wave number, the wave frequency remains constant, as required by mass conservation. Equation (12) indicates that the jet impingement force is oscillatory in time with frequency f, and it increases in the z direction. If the impact surface is positioned past the breakup length, then a series of droplet impacts will occur.

V. FORCE INDUCED BY DROPLETS

The impact force of a single droplet has been experimentally investigated and modeled in several studies [50–54]. These studies reveal that the impact force-time history is characterized by a rapid increase to a maximum followed by a progressively longer decay to zero. For droplet impacts where viscous effects are negligible ($\mathrm{Re}_D = \rho v D/\mu \gtrsim 200$), the peak force occurs at a nondimensional time of $\tilde{t} = tv/D = 0.15$, where $\tilde{t} = 0$ corresponds to the moment of impact, and it reaches a peak magnitude of approximately $\tilde{F} = F_{\mathrm{drop}}/\rho v^2 D^2 = 0.85$ [53]. Note that a tilde denotes quantities normalized using the droplet diameter D, and a caret denotes quantities normalized using the initial jet diameter d_0. The droplet impact time duration (total time of loading) occurs for approximately $\tilde{t} \approx 2$. In this regard, peak force is attained rapidly, and thus the force profile is highly asymmetric in time.

In terms of modeling the time-dependent impact force, studies have predicted the early-time (before peak) force to scale as $\sqrt{t}$ [54]. This early-time behavior has been confirmed in recent experimental studies [52,53]. Unfortunately, to date, an exact theoretically derived model does not exist for the entire time-dependent droplet impact force. Recent work [53], however, shows that the post-peak behavior is well-described as a lumped system and thus accurately approximated with an exponential decay model. In Ref. [53], a semiempirical model that incorporates the early-time $\sqrt{t}$ dependence and the observed exponential post-peak decay is constructed. The model equation for the entire time-dependent loading of droplet impacts with negligible viscous effects is expressed as

$$\tilde{F}_{\mathrm{drop}}(\tilde{t}) = \sqrt{\frac{1000\pi\tilde{t}}{243}} e^{\frac{-10\tilde{t}}{3}}, \tag{14}$$

and it is applicable over the range of droplet Reynolds numbers ($280 \lesssim \mathrm{Re}_D \lesssim 30\,000$) and Weber numbers ($37 \lesssim \mathrm{We}_D = \rho D v^2 / \sigma \lesssim 6400$). As indicated by experiments, this model equation satisfactorily predicts the force induced by a wide range of droplet impacts [53]. Equation (14) is restricted to droplets that are spherical upon impact. Droplets that are oblate or prolate upon impact exhibit different profiles from spherical droplets. With respect to a spherical droplet impact, oblate impacts have shorter time durations and higher peak forces, while prolate impacts exhibit longer time durations and lower peak forces. Within this context, the areas under the profiles of spherical, oblate, and prolate impacts are approximately the same.

Another important aspect of characterizing a droplet impact is its impulse. The impulse is the area under a force-time profile, and physically indicates the amount of momentum exchanged during a collision. The area under the curve [Eq. (14)] is, by design, equal to the droplet momentum just before impact. This implies that the inertially dominated droplet impact is modeled by a perfectly inelastic collision. In this case, the impulse is expressed as

$$\tilde{I}_{\mathrm{drop}} = \int_0^\infty \tilde{F} \, d\tilde{t} = \frac{\pi}{6}. \tag{15}$$

As specified, the value $\pi/6$ is equal to the momentum of the drop mv (where m is the droplet mass) normalized by $\rho D^3 v$. Note that if the droplet rebounds from the surface with the same velocity but in the opposite direction, then the impulse will be twice that given by Eq. (15). In this context, the droplet impact is perfectly elastic. Superhydrophobic surfaces allow droplets to rebound [55], and consequently, the force induced by this type of impact differs fundamentally from that given by Eq. (14). It is important to note that Eqs. (14) and (15) model droplets impinging and adhering onto solid dry surfaces. One may wonder if these expressions, which characterize a single droplet impact, may be extended to a continuous train of droplet impacts emanating from a liquid jet, like that depicted in Fig. 1(c).

One important feature of droplet trains is the presence of a liquid film atop the impact surface. It is likely that after the first droplet impact, a film of liquid will pool about the impact location. Droplets impacting a deep pool ($L_p \gg D$, where L_p is the pool depth) [see Fig. 1(c)] that have sufficient speed will create a Worthington jet [56]. In contrast, droplets impacting a shallow pool, $L_p < D$, typically splash with an upward-propagating crown [10,14,57], which often fragments into smaller droplets. The force induced by water droplets impacting various depths of water has been measured by Yu and Hopkins using an acoustic-based wavelet deconvolution method [51]. Their results show that the force associated with capillary waves and the ascending crown tend to be negligible compared to the force induced by the initial droplet impact. Qualitatively, the presence of a shallow pool increases the peak force and time to reach peak force, making the force profile more symmetric. In addition, the presence of a pool increases the observed impulse. This increased impulse indicates that the impact tends toward conditions in which the drop momentum is redirected upward. This is indeed the case for Worthington jets as liquid is sent upward after the drop coalesces with the deep pool. In general, however, for $L_p \to 0$, the shallow pool force profile approaches the dry-surface force profile.

If the pool depth is very shallow and has negligible effects on the droplet force profile, then the force induced by a train of droplets can be modeled by a series of single droplet impacts via Eq. (14). If equal-sized droplets of diameter D are formed at the breakup length L_b, at a rate f, and one droplet is produced per wavelength, then the force induced by a series of droplet impacts is given by

$$\hat{F}_c(\hat{t}) = \sum_{n=1}^{N} \hat{F}_n(\hat{t}), \tag{16}$$

where the subscript c refers to the scenario depicted in Fig. 1(c), n corresponds to the droplet number, N is the total number of droplets, and $\hat{F}_n = F_{\mathrm{drop}}/\rho v_0^2 d_0^2$, but shifted in time by the amount $\hat{t}_n = v_0(n-1)/(d_0 f)$. Explicitly, $\hat{F}_n$ is the droplet impact force normalized by the jet parameters
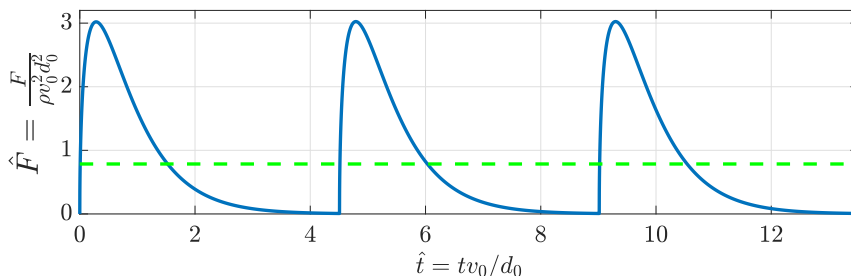
FIG. 3. Force induced by a droplet train according to the Rayleigh mode (solid blue), and force induced by a steady-state jet (dashed green), shown for three cycles. The area under each profile (impulse) is approximately equal (i.e., both scenarios exchange the same cycle-averaged momentum with the surface). Due to its discrete nature, the droplet train experiences a greater peak force than the steady-state jet.

and is written as

$$\hat{F}_n(\hat{t}) = \left(\frac{v}{v_0}\right)^{5/2} \left(\frac{D}{d_0}\right)^{3/2} \sqrt{\frac{1000\pi\hat{t}}{243}} \, e^{\frac{-10vd_0\hat{t}}{3v_0D}}, \tag{17}$$

where $D = (3\pi d^2/k)^{1/3}$ is the droplet diameter, with v, d, and k given by Eqs. (8), (9), and (13), respectively. This form ensures that mass conservation is satisfied assuming that one droplet is produced per wavelength. If indeed the impact is perfectly inelastic, then Eq. (16) also satisfies momentum conservation as the axial momentum of a section of the jet (which has the volume of the drop) becomes the droplet momentum that is then transferred to the surface upon impact. Accordingly, the impulse of one droplet in the series is equal to the impulse of the continuous (or wavy) jet of equal volume. This is perhaps not surprising since in all three scenarios in Fig. 1 the same momentum exits the nozzle, and thus by momentum conservation the same momentum must be exchanged with the surface. Figure 3 shows three cycles of the droplet train force profile given by Eq. (16), based on the Rayleigh mode, along with the steady-state force profile given by Eq. (7). Note that the impulse given by Eq. (15) is evaluated from $t = 0$ to $t \rightarrow \infty$, and thus in order for the droplet train impulse Eq. (16) to be exactly equal to the steady-state (or wavy jet) impulse, one must allow $t \rightarrow \infty$. This indicates that over one cycle, from t_n to t_{n+1}, the areas under each curve are only approximately equal. To highlight this, the impulses of each profile determined for the first cycle in Fig. 3, from $\hat{t} = 0$ to $\hat{t} = v_0/(d_0 f)$, differ by 0.12%. Therefore, the impulses experienced by the two scenarios over one cycle are approximately equal. In light of this subtlety, momentum conservation requires the droplet train force profile and the steady-state force profile to exhibit the same impulse (as $t \rightarrow \infty$). Due to the droplet train's discrete nature, there exists periods of approximately zero induced force. Therefore, in order to satisfy momentum conservation, there must be a greater peak force induced by the droplet train than the steady stream. This is apparent in Fig. 3, where the peak force is greater by a factor of 3.85. Note that for decreasing wave number (i.e., longer wavelengths), droplets become larger and are spaced farther apart, resulting in higher peak forces. This may be appealing for industrial use. However, in practice longer wavelengths are difficult to achieve due to secondary swellings [44]. It is worth noting that a previous study has reported that the peak force induced by a droplet is 3.5–4 times greater than that of the continuous stream counterpart [58]. In this study, the force induced by free-falling, dripping droplets was measured and compared to the theoretical impact force of a continuous jet, Eq. (7). The experiment conducted in [58] differs from the experiments presented in this paper as direct force measurements of Rayleigh jets are conducted for each of the possible outcomes (i.e., a steady jet, a wavy jet, and a droplet train), and they are compared with novel force models [i.e., Eqs. (12), (16), and (17)].

The jet and droplet acceleration due to gravity, via Eq. (8), is incorporated into Eqs. (10), (12), (16), and (17). This indicates that the velocities of the steady-state jet, the wavy jet, and the droplet
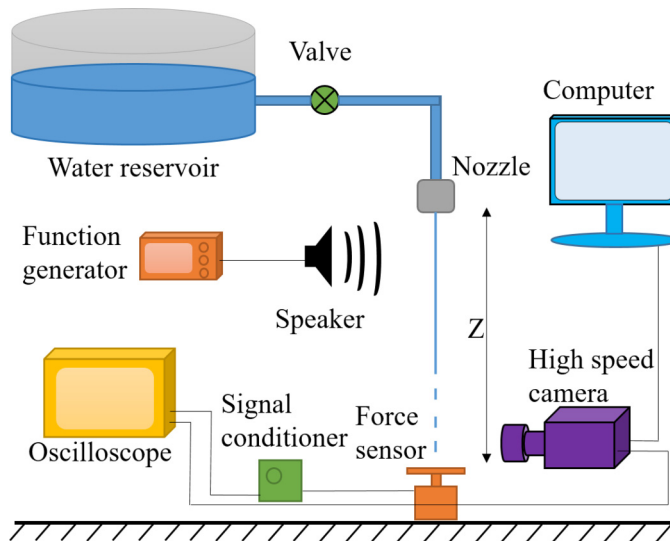
FIG. 4. Schematic of the experimental setup. A Rayleigh jet is formed and impacts normal to a piezoelectric force sensor. A speaker stimulates the free surface to form a wavy jet/droplet train.

train are equal upon impact, given that the nozzle to plate distance and nozzle exit conditions are equivalent. Similarly, Eqs. (10), (12), and (16) are all normalized with respect to the jet inertial parameters enabling direct comparison. The expressions characterizing the induced force of steady-state jets, wavy jets, and droplet trains demonstrate the roles of impulse, peak force, and momentum conservation. Many industrial applications (and natural phenomena) exhibit these types of Rayleigh jet impacts, and thus the accuracy of the above models is of interest. Experimental comparisons with the given models are now provided.

VI. EXPERIMENTAL SETUP AND PROCEDURES

A precisely reamed aluminum nozzle with a diameter $d_n = 1.65$ mm and length $L_n = 0.38$ mm is used to form our Rayleigh jet. A 260-mm-diam reservoir supplies water to the nozzle through a 13-mm-diam hose; see Fig. 4 for a schematic of the experimental setup. Once formed, the jet travels in the direction $\vec{g}$ and impacts a piezoelectric force sensor (PCB model 209C11), located a distance $Z = 106$ mm from the nozzle exit. The bottom of the force sensor is threaded to a large steel plate. On top of the sensor rests a 17.9-mm-diam polyoxymethylene plastic impact plate and it is the target for the impinging jet. Note that a 12.3-mm-diam aluminum impact plate is used for the wavy jet experiments. The excitation voltage necessary for the force sensor is supplied by a PCB model 482 signal conditioner. A Lecroy Wavesurfer 64MXs-B oscilloscope sampling at 100 kHz is used to acquire the force sensor response. A Photron SA4 Fastcam is used to take high-speed photographs of the impinging jets at a frame rate of 13 500 fps and an exposure time of 74 μs. The camera is positioned next to the force sensor revealing the last 15 mm of the jet before impact. Time is synchronized between the camera and force sensor through the oscilloscope. A 0.2 W speaker is placed perpendicular to the stream at the nozzle exit to provide wave-number stimulation (only used for the wavy jet and droplet train experiments). The orientation of the speaker perpendicular to the jet assures negligible momentum is added to the jet by the sound wave. A function generator provides the speaker with a sinusoidal stimulation frequency of 340 Hz and imposes a peak-to-peak voltage of 1.5 and 20 V for the wavy jet and droplet train experiments, respectively. The imposed frequency corresponds to a wave number of $kR = 0.634$ at impact. This is close to the wave number of the Rayleigh mode (i.e., $kR = 0.697$); see Fig. 2. The camera field of view is small relative to

the length of the jet. This allows one to assume a constant wave number at the impingement zone of the wavy jet. With this field of view, approximately two wave crests are observed at any given time. By tracking the free surface, the wave growth rate β may be determined as well as the equivalent initial wave amplitude a. Once obtained, these parameters permit use of Eq. (12) to compare with experimental results. If one droplet is produced per wavelength, then the droplet diameter would be 2.7 mm. However, satellite droplets form in between primary drops, and thus the primary droplet diameter is smaller than this value. In general, it is difficult to precisely measure the droplet diameter as the droplet oscillates between an irregular prolate and oblate shape after pinch-off. The droplet impact velocity is approximately equal to the impact velocity of the steady state and wavy jet as indicated by high-speed images and position-tracking software.

Nozzle exit velocity is controlled by the hydrostatic water level in the tank. Flow-rate measurements determine the nozzle exit velocity to be $v_0 = 1.84$ m/s. The velocity change due to reservoir drainage is negligible: after 60 s of continuous flow, the velocity decreases by about 1%, corresponding to a 2% decrease in induced force (i.e., force scales as v^2 in the inertial limit). The duration of one droplet impact or one wave impact occurs on a millisecond time scale. Therefore, the change in velocity during the experiment is much smaller than 1%, permitting a constant flow velocity assumption. According to images taken at the nozzle exit, the diameter of the jet contracts to $d_0 = 1.56$ mm, corresponding to a contraction ratio of $\chi = 95\%$. This decrease in jet diameter is consistent with the study of Gavis and Modan [46]. The density and viscosity of the water are $\rho = 998$ kg/m^3 and $\mu = 1.0$ cP, respectively. The Reynolds and Weber numbers of the jet are Re $= \rho d_0 v_0 / \mu = 2860$ and We $= \rho d_0 v_0^2 / \sigma = 73$, respectively. These ratios identify the inertial force as dominant compared to viscous and surface tension forces. With the ambient gas being stagnant air, this Weber number satisfies Eqs. (1) and (2), and therefore the jet is considered to be within the Rayleigh regime.

To mitigate transient effects associated with mechanically opening the nozzle supply valve, a sheet metal plate is positioned in front of the stream close to the force sensor while opening the valve. This diverts the stream from the sensor and allows the jet to reach steady state. After about 2 s, the shielding plate is quickly removed, allowing the jet to freely impinge the force sensor. In this process, a liquid globule at the fore of the jet always develops (see the Supplemental Material [59]). Although undesirable, the duration of the transient effect associated with the globule is much shorter than that of opening the valve.

VII. RESULTS AND DISCUSSION

Images of the steady-state jet, the wavy jet, and the droplet train are shown in Fig. 5, while the force induced by these impacts is shown in Fig. 6 for a duration of 60 ms. The flow conditions exiting the nozzle in all three scenarios are identical, as is the nozzle to plate distance. The state of the jet upon impact is governed by the artificial stimulation induced by the audio speaker. The series of images displayed in Fig. 5 reveal the jet evolution in 12 increments of 370 μs for the steady state and wavy jet, and eight increments of 593 μ s for the droplet train. These durations correspond to slightly more than one time period. Notice that the steady-state jet [Fig. 5(a)] appears to be time-invariant as expected, while the wavy jet [Fig. 5(b)] exhibits a series of wave impacts. The droplet train [Fig. 5(c)] displays a series of droplet impacts. To correlate the time in which the impacts in Fig. 5 occur with their corresponding force, green-shaded regions are outlined in Fig. 6. These regions allow the force to be directly compared with Fig. 5. Supplemental movie files show how the force evolution compares with the images of the jets' impact [59].

A. Steady-state jet

Figure 6(a) shows the force induced by the steady-state jet. Here, the transient effect associated with the globule at the fore of the jet is apparent from 0 ms (initial impact) to about 3 ms. Here a large increase in force is observed due to the sudden redirection of momentum from the axial to
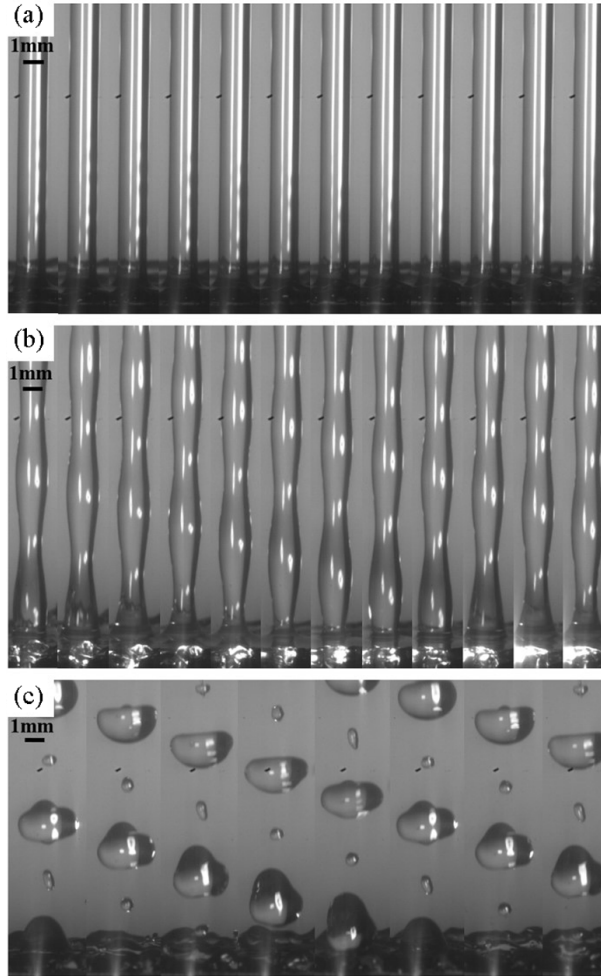
FIG. 5. High-speed images of the normal impingement of Rayleigh jets: (a) steady-state jet, (b) wavy jet, and (c) droplet train. The progression of images is from left to right in increments of 370 μs (a), (b) and 593 μs (c). The time in which these impacts occur corresponds to the shaded green regions in Fig. 6.

radial direction of the jet. Once the transient effect subsides, the force induced by the steady-state jet remains close to the inviscid prediction (dashed green line), while slight deviations exist presumably due to random oscillations of excess liquid on the plate. The steady-state force given by Eq. (10) is 8.2 mN and compares well with the experimental results immediately following the transient. As time increases, however, the force increases slightly due to mass accumulation on the force sensor. High-speed images reveal that the excess liquid adheres to the plate and does not flow off the edge. Therefore, to account for the additional weight on the force sensor, a mass accumulation term is included in Fig. 6(a), represented by a dotted orange line. The additional weight is simply the accumulated liquid given by $\rho \dot{V} g t$, where $\dot{V}$ is the jet flow rate. This modification to Eq. (10) follows the data trend.

B. Wavy jet

The force induced by the wavy jet is shown in Fig. 6(b). As is apparent, the force oscillates in accordance with the sinusoidal free-surface radius at the fixed plate location. Physically, as the jet's
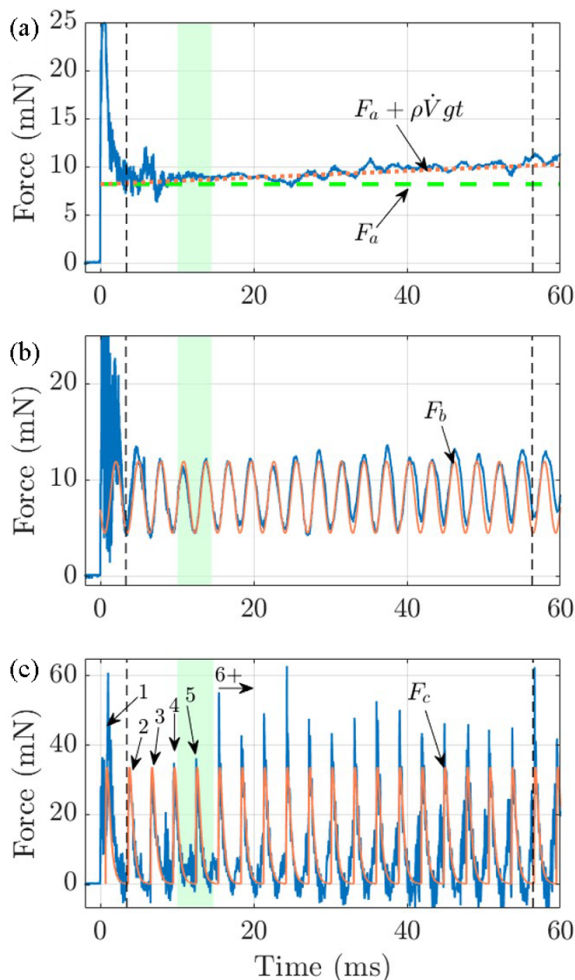
FIG. 6. Force induced by Rayleigh jets: (a) steady-state jet, (b) wavy jet, and (c) droplet train. Arrows indicate model predictions (orange/green), e.g., F_a, F_b, and F_c from Eqs. (10), (12), and (16), respectively. The (dashed black) lines indicate integration bounds.

cross-sectional area expands, the plate diverts more momentum, thus corresponding to a greater force. Equivalently, when the area contracts, less momentum is diverted by the plate driving the force toward its lower bound. The force amplitude is approximately 3.7 mN and fluctuates about the steady-state jet force. The average oscillation frequency of the peak-to-peak force is 340 Hz, corresponding to the stimulation frequency. In contrast to the steady-state jet, the excess liquid in the wavy jet flows off of the impact plate due to the smaller diameter plate used. Therefore, the linearly dependent mass accumulation term used in Fig. 6(a) is not required. To use Eq. (12) to compare with the experiments, the wave growth rate β and the equivalent initial wave amplitude a must be determined.

High-speed images and edge detection software were used to record the free surface of the wavy jet. The free surface of the jet is measured at fixed z locations, from $t = 10$ to 30 ms, representing about six cycles. The axial locations range from $z = 91$ to 105 mm in 26 increments of about 0.55 mm. Recall that in the laboratory reference frame the wavy jet oscillation amplitude increases with axial distance. A linear regression performed on the observed amplitudes was used to estimate
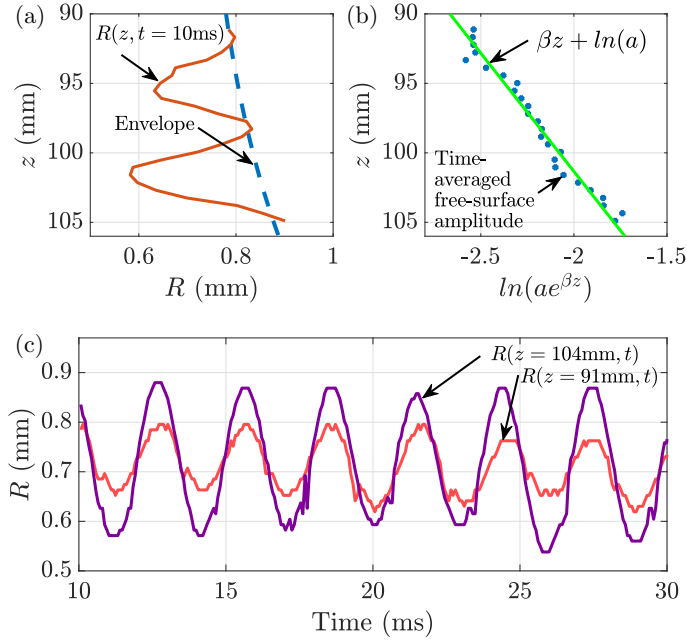
FIG. 7. Wavy jet free-surface profile. (a) The free-surface along the axial direction z, at $t = 10$ ms (red line), with an envelope representing the time-averaged amplitude (dashed blue line). (b) The time-averaged amplitude of z locations near the plate (blue dot), with the line of best fit (green line). (c) The free surface with respect to time at locations $z = 104$ mm (purple line) and $z = 91$ mm (red line).

their growth rate and equivalent initial wave amplitude. Figure 7(a) shows the free surface at $t = 10$ ms, with an orange line, where two waves are observed. It is clearly noticeable that the amplitude of oscillation increases with the z direction. The time-averaged amplitude is recorded and plotted in Fig. 7(b) with blue dots. The line of best fit, using linear least squares, is presented with a green line. This yields $\beta = 58.7 \, \text{m}^{-1}$ and $a = 3.52 \times 10^{-7}$ m for the model $\beta z + \ln(a)$. With these parameters, the time-averaged envelope is plotted in Fig. 7(a) with a dashed blue line. Figure 7(c) shows the free-surface radius with respect to time for axial locations of $z = 91$ and 104 mm, respectively. Notice that the $z = 104$ mm location oscillates with a greater amplitude (by a factor of 2.01). This is due to the exponentially increasing free-surface radius along the z direction, as predicted by Rayleigh jet theory. The mean free-surface radius is 0.71 mm, which is also the radius obtained for the steady-state jet. These values fall within 3% of the predicted radius via Eq. (A11). The edge detection software also allows us to measure the jet wavelength, which is $\lambda = 6.61$ mm. This value is within 4% of that expected through Eq. (13). In addition, the wave frequency may be measured by the frequency of the peak-to-peak free-surface amplitude at a fixed z distance. This method is in agreement with the artificially induced frequency. Note that the droplet impact frequency may also be measured in a similar manner.

The predicted oscillatory force, through Eq. (12), is plotted with an orange line in Fig. 6(b). Equation (12) compares well with the measured force, containing the same frequency and approximately the same amplitude. Note that the phase in Eq. (12) is arbitrary, depending only on the time in which the analysis starts, thus the phase is chosen to coincide with the measurements, and it is set to $\zeta = 1.39\pi$. The wave amplitude at impingement is roughly 30% of the jet radius, which is rather large. Despite the small wave-amplitude assumption considered in deriving Eq. (12), there is good agreement with the theoretical prediction and the measurements. At $t = 0$ ms, the transient effect is apparent and occurs along a similar time duration to that for the steady-state jet. The droplet train
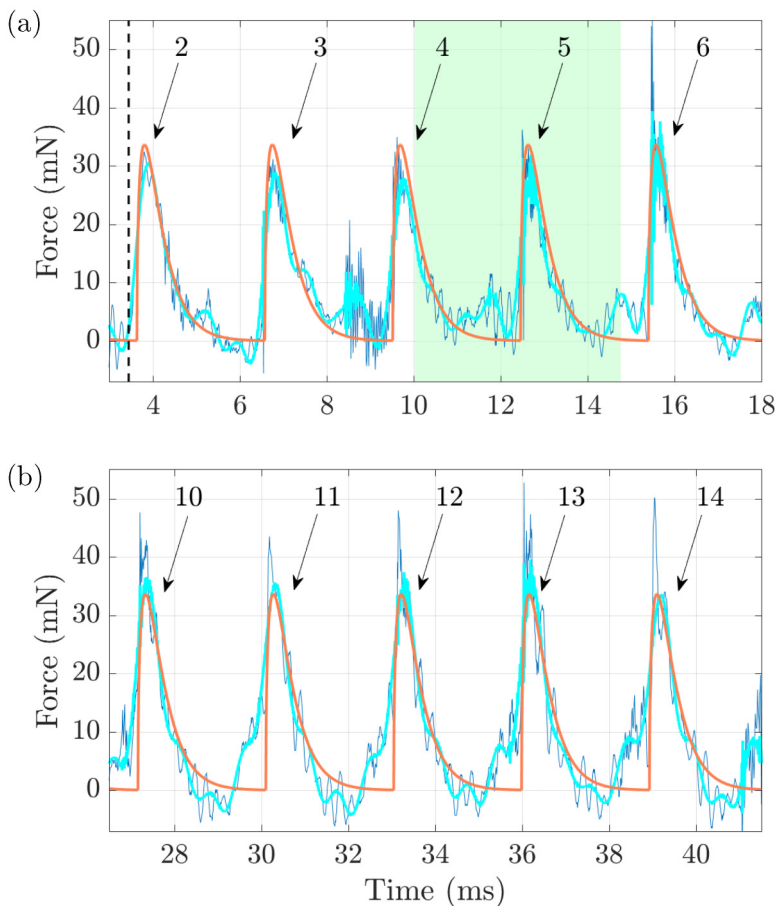
FIG. 8. Force induced by the droplet train (blue-raw), and (cyan-filtered) for primary droplet impact numbers 2–6 (a) and 10–14 (b). The force predicted by Eq. (16) is shown in orange. For successive impacts (b), the presence of a liquid pool increases the peak force and alters the force profile toward symmetric conditions about the peak force.

does not exhibit the same transient effect as the continuous jets, rather two droplets at the fore of the train impact at similar times.

C. Droplet train

High-speed footage of the droplet train reveals that an irregularly shaped large droplet first impacts the plate away from the center (at roughly $r = 4$ mm; see the Supplemental Material [59]). Therefore, the first primary droplet and all subsequent droplets impact the force plate center. The first irregular droplet is the remnant of the transient effect associated with rapidly removing the shielding plate as previously described. In Fig. 6(c), the primary droplet force profiles are labeled in sequence (i.e., 1, 2, 3, etc).

Coincident with the irregular drop and the first primary drop, the force sensor shows a long period of induced force, from $t = 0$ to 3 ms, with two distinct peaks, the first being from the irregular drop and the second caused by the first primary drop. The ensuing four droplet impacts exhibit similar force characteristics to one another. These are labeled as 2–5 in Fig. 6(c) and also in Fig. 8, which is a magnified version of Fig. 6(c). For each of these impacts, the force-time profiles exhibit a rapid

increase in force, reaching a maximum of about 30 mN. This is followed by a longer fall-time to zero force. The total loading time for each droplet is about 3 ms. Comparatively, peak force is attained rapidly, just 200 μs from initial impact. The characteristics of these four *initial* force profiles are similar to the profiles of individual droplet impacts onto dry surfaces [53]. The profiles of these impacts are clearly shown in Fig. 8(a), as well as the profiles of successive drops, shown in Fig. 8(b). After the initial impacts (2–5), the successive force profiles (labeled as 6+) exhibit greater peak forces while becoming more symmetric about the time of peak force. This effect is attributed to the presence of a growing pool of excess liquid [51]. High-speed images show that most of the liquid from the droplet train remains on the plate, creating a pool about the impact location. The pool depth varies chaotically as droplets impinge, but in general the pool depth at the plate circumference is larger than at its center. Qualitatively, the presence of a pool increases the peak force and causes the force profile to become more symmetric about the time of peak force. These observations coincide with the study of Yu and Hopkins [51], where the authors measure the force of single droplets impinging a pool of water. It is therefore asserted that the force induced by droplet trains is influenced by shallow pools.

The physical rationale for the increased peak force and the altered force profile (toward conditions of symmetry) due to the presence of a pool is that the water layer fundamentally changes the transmission of momentum from the droplet to the surface. In the case of a dry surface, all of the momentum mv is transmitted to the surface; see Eq. (15). Due to the compliant nature of the water layer, a portion of the axial momentum is redirected upward. In this context, the impact behaves toward conditions of a perfectly elastic impact where all of the momentum is reflected. For such an idealized impact, the total impulse experienced by the surface would be $2mv$ and the force profile would be symmetric about the peak force. Due to the increased impulse (i.e., the area under force-time curve), the peak force increases correspondingly as long as the time durations are approximately equal. It is evident from Fig. 8 that with successive impacts, the individual force profiles deviate from the dry-surface profile, given by Eq. (14). Therefore, the effects associated with the growing pool of liquid begin to invalidate the perfectly inelastic collision assumption incorporated in Eq. (16). Accordingly, as the pool depth grows, the force predicted by a series of individual droplet impacts, via Eq. (16), becomes less accurate.

The force predicted by Eq. (16) is plotted in Figs. 6(c) and 8 with an orange line. Due to the first irregular transitory drop, Eq. (16) is shifted in time by 0.7 ms to coincide with the measurements. It is apparent that Eq. (16) satisfactorily predicts the cyclic response of 340 Hz. However, the peak force of successive impacts (6+) is underestimated. Again, this is attributed to the pool, as the profiles of primary drops 2–5 compare reasonably well with Eq. (16), exhibiting a fast rise to maximum force followed by a progressively slower transition to zero. In all of the individual profiles, however, high-frequency oscillations exist.

Superimposed oscillations hamper the underlying response of the droplet train. This effect has been found in other droplet impact force studies [50–53]. The oscillations are attributed to the resonant vibration of the force sensor system [60]. The undesired ringing can be mitigated by reducing the droplet impact velocity, or by spectrally filtering the response. In addition, for these experiments plates of low mass are used, which reduce the influence of superimposed oscillations [60]. The measured forces in Figs. 6(a)–6(c) are not filtered, revealing the sensor's direct response. The droplet train data presented in Fig. 8 are filtered with a low-pass filter attenuating frequencies above 2000 Hz (cyan line). The steady state and wavy jet exhibit oscillations as well, due to the suddenly applied load, but they diminish at about $t = 3$ ms; see Figs. 6(a) and 6(b). Unlike the continuous jets, however, each droplet impact in Figs. 6(c) and 8 appears to induce its own oscillations, therefore facilitating continuous ringing. Despite the ever-present oscillations, their amplitudes are small, roughly 15% of the peak force magnitude. Note that the pool of water randomly fluctuates and thus also introduces an additional, irregular force.

In contrast to the steady-state jet results, which show a linearly increasing force attributed to the accumulated liquid, the droplet train response does not appear to exhibit such a feature. One possible explanation for this is that the weight of the accumulating mass is insignificant compared to the

large force induced by the droplets and their associated ringing. In addition to these abnormalities (compared to a single droplet impact onto a dry surface), the force dips below 0 mN, indicating that an upward force on the sensor is applied. According to high-speed images, after a droplet impinges, its liquid travels radially from the center colliding with the annular globule at the perimeter. It is suspected that capillary forces prevent the liquid from flowing off the plate edge, thus allowing liquid to accumulate and preventing further radial flow. Due to this restriction, a component of radial momentum is then directed upward only to yet again be bound by surface tension. Despite the greater peak forces experienced by successive droplet impacts, the negative force experienced by the ascending liquid renders a net momentum change of zero. Therefore, the impulse experienced by successive droplet impacts may be regarded as equivalent to primary drops.

In Fig. 5(c) and in the Supplemental Material [59], the impingement of satellite droplets in-between primary droplets is clearly observed. The satellite drops are equally spaced in between primary drops and have a diameter of roughly 0.65 mm. With this diameter and equal impact velocity as primary drops (i.e., $v = 2.34$ m/s), the peak force of satellite drops, via Eq. (14), is 1.96 mN. This small level of force is hardly noticeable in Figs. 6(c) and 8, especially among the ringing. Due to this, the force of satellite drops can be regarded as negligible compared to primary drops.

One additional artifact of the droplet train is that the droplets are not spherical upon impact. Indeed, the drops oscillate between an irregular prolate and oblate shape. Upon impact, the drops are slightly prolate. This indicates that the duration of momentum transmission from the drop to the surface is longer compared to a perfectly spherical drop. The consequences of this are a decrease in peak force and an increase in time duration. Although Eq. (16) suitably predicts the force induced by the initial droplets impacts, Fig. 8(a) shows that the peak force falls slightly lower than that predicted by Eq. (16). Despite this and the inconvenient ringing, Eq. (16) compares reasonably well with the measurements.

D. Impulse and momentum conservation

The jet momentum is assessed by integrating the force with respect to time (i.e., impulse). It is important that the domain of integration covers an integer number of cycles for the wavy jet and droplet train. In this way, the quadrature is representative of the total number of waves or drops that impact the surface. The force is integrated over 18 cycles for the wavy jet and droplet train. The dashed black lines in Fig. 6, which represent the lower and upper bounds of integration, are at $t = 3.5$ and 56.4 ms, respectively. The momentum of the steady-state jet is also assessed on the same domain. The measured impulse of the steady-state jet, the wavy jet, and the droplet train is $I_a = 5.00 \times 10^{-4}$ N s, $I_b = 4.70 \times 10^{-4}$ N s, and $I_c = 4.99 \times 10^{-4}$ N s, respectively. It appears that the impulse exerted by the steady-state jet and the droplet train are similar due to the accumulated mass on the sensor. In contrast, the wavy jet has a slightly smaller impulse. If the contribution from the mass accumulation term is subtracted from the steady-state jet impulse I_a, then the steady-state jet impulse is 4.46×10^{-4} N s. This value is close to the impulse of the wavy jet, differing by about 5%. In light of the subtleties surrounding the accumulated mass, it may be regarded that in all three scenarios the plate diverts the same n-cycle momentum. This should not be surprising as the same momentum exits the nozzle. Only the planar area of the liquid arriving at the plate differs between the scenarios. In this regard, the only inertial difference is the duration of momentum transmission from the liquid to the surface. This statement essentially outlines a tradeoff between a constant steady momentum flux (a) and discrete packets of momentum arriving in short bursts (c), with the momentum imparted by the wavy jet (b) being an intermediate scenario.

E. Steady-state jet versus droplet train

The normalized force induced by the steady-state jet (green line) and the droplet train (blue line) is shown in Fig. 9. Here, the remarkable difference is with respect to the force signature. Despite
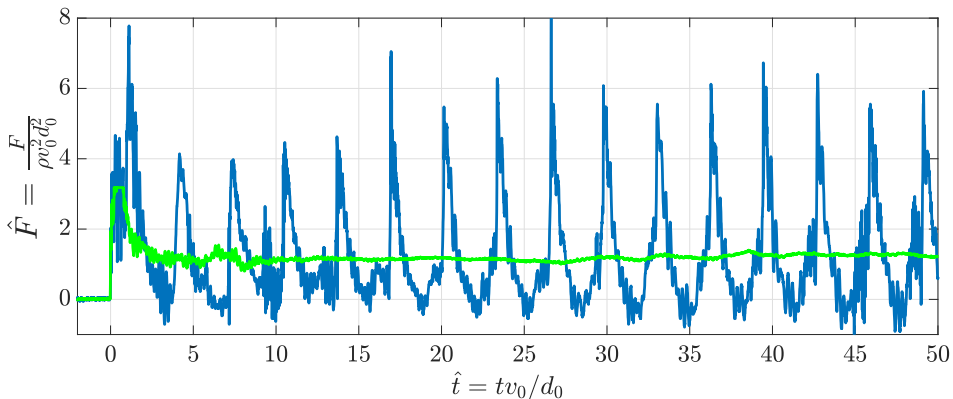
FIG. 9. Normalized force of the steady-state jet (green) and droplet train (blue). Both jets have identical nozzle flow conditions, yet peak force induced by the droplet train is over three times greater. Both profiles exhibit approximately the same impulse, as required by momentum conservation.

the identical nozzle flow conditions and equal nozzle to plate distance, the peak force induced by the droplet train is significantly greater than the steady-state jet. Nevertheless, there exist periods of approximately zero induced force for the droplet train. For the first several primary droplets, before the pool affects the force profile, the peak force is about three times greater. For the successive primary drops, the peak force is about five times greater than the steady-state jet. For industrial applications such as waterjet cutting or surface cleaning, it may be advantageous to use a droplet train in lieu of a steady-state jet due to the greater peak forces experienced by the impingement surface. Although there is a considerable difference in force between these two scenarios, their n-cycle momentum is approximately the same, as required by momentum conservation.

VIII. CONCLUSION

The normal force induced by Rayleigh jets is measured with a high-sensitivity piezoelectric sensor. A high-speed camera records the jets' impingement and their free-surface profile. The force of these jets is measured for identical nozzle flow conditions and for equal nozzle to plate distance. Upon impingement with the surface, the state of the jet is categorized as either a steady-state jet, a wavy jet, or a droplet train. The wavy jet and droplet train are created by artificially stimulating the jet with an audio speaker placed next to the nozzle exit. The prescribed frequency excites wave numbers associated with fast wave growth rates allowing wave amplitudes to be larger than if left to occur naturally.

An accurate force model for wavy jets, Eq. (12), is presented using the spatial form of Rayleigh jet theory. The level of agreement between the model and experimental results is excellent, validating the model's accuracy. In addition, a series of single droplet impact force profiles are combined to provide a model for the force of droplet trains. This model, which is based on momentum conservation, accurately captures the force induced by the initial primary droplets; however, as a liquid pool develops about the surface, the force changes fundamentally. The pool increases the peak force and delays the rise time, making the profile more symmetric.

Compared to the steady-state jet, the droplet train exerts a significantly greater peak force. However, due to its discrete nature, the droplet train also exhibits periods of approximately zero induced force. While its force varies periodically, its n-cycle momentum may be regarded as equivalent to the steady-state jet case, i.e., conservation of momentum. It may be more beneficial for industrial applications to use a train of droplets instead of continuous jets, due to the greater forces experienced by the impingement surface. The normal impingement of Rayleigh jets demonstrates

the roles of inertia, impulse, and momentum conservation, while providing a fundamental platform for the examination of impact force.

APPENDIX: JET VELOCITY AND RADIUS INFLUENCED BY GRAVITY

In this Appendix, we show how gravity accelerates the falling jet velocity $v = v(z)$ and consequently contracts its radius $R = R(z)$. It is assumed that the jet is in a steady state and travels along the axial direction z. Similarly, gravity acts in this direction with magnitude g. The jet has a nozzle exit velocity of v_0, and it exhibits uniform flow [i.e., $v = v(z)$]. It is also assumed that the jet Reynolds number is sufficiently high, such that viscous effects are negligible. The steady Bernoulli equation may be applied along a streamline of the jet, which we take to be the z axis. Points z_1 and z_2 are two points on the z axis, where $z_1 = 0$ is the nozzle location and $z_2 = z$ is an arbitrary axial location where the jet velocity and radius are to be determined. Applying Bernoulli's equation to these points, we have

$$p_1 + \tfrac{1}{2}\rho v_0^2 = p_2 + \tfrac{1}{2}\rho v(z)^2 - \rho g z, \tag{A1}$$

where $v(z) = v_2$. The pressures may be determined through the Young-Laplace equation:

$$p = p_0 + \sigma \nabla \cdot \vec{n}, \tag{A2}$$

where p_0 is the ambient pressure and $\vec{n}$ is the free-surface normal vector (see Fig. 1). The $\nabla \cdot \vec{n}$ term is the free-surface curvature and may be expressed in terms of the two principal radii of curvature, R_1 and R_2, as

$$\nabla \cdot \vec{n} = \left(\frac{1}{R_1} + \frac{1}{R_2} \right). \tag{A3}$$

It is assumed that the azimuthal curvature $1/R_1 = 1/R(z)$ is much greater than the axial curvature $1/R_2$, permitting

$$\nabla \cdot \vec{n} \approx \frac{1}{R(z)}. \tag{A4}$$

The Bernoulli equation now becomes

$$\frac{\sigma}{R_0} + \frac{1}{2}\rho v_0^2 + \rho g z = \frac{\sigma}{R(z)} + \frac{1}{2}\rho v(z)^2. \tag{A5}$$

Solving for the normalized velocity $v(z)/v_0$, we obtain

$$\frac{v(z)}{v_0} = \left[1 + \frac{1}{\mathrm{Fr}}\frac{z}{R_0} + \frac{4}{\mathrm{We}}\left(1 - \frac{R_0}{R(z)} \right) \right]^{1/2}, \tag{A6}$$

where We and Fr are the previously defined Weber number and Froude number, respectively. By mass conservation, the flow rate at the nozzle $z = z_1$ is equal to the flow rate at the location $z = z_2$:

$$\pi R_0^2 v_0 = \pi R^2 v. \tag{A7}$$

Rearranging for the normalized radius, we have

$$\frac{R(z)}{R_0} = \left(\frac{v(z)}{v_0} \right)^{-1/2}, \tag{A8}$$

which corresponds to

$$\frac{R(z)}{R_0} = \left[1 + \frac{1}{\text{Fr}}\frac{z}{R_0} + \frac{4}{\text{We}}\left(1 - \frac{R_0}{R(z)}\right)\right]^{-1/4}. \tag{A9}$$

If capillary effects can be neglected (i.e., We $\to \infty$), then Eqs. (A6) and (A9) reduce to

$$\frac{v(z)}{v_0} = \left[1 + \frac{1}{\text{Fr}}\frac{z}{R_0}\right]^{1/2} \tag{A10}$$

and

$$\frac{R(z)}{R_0} = \left[1 + \frac{1}{\text{Fr}}\frac{z}{R_0}\right]^{-1/4}. \tag{A11}$$

Notice that the jet velocity increases with the square root of the axial distance z, and correspondingly the radius decreases along the z direction with power $-1/4$. Furthermore, if gravitational effects are assumed negligible (i.e., Fr $\to \infty$), then the jet velocity and radius remain unchanged.

---

[1] H. Glover, T. Brass, R. Bhagat, J. Davidson, L. Pratt, and D. Wilson, Cleaning of complex soil layers on vertical walls by fixed and moving impinging liquid jets, J. Food Eng. **178**, 95 (2016).

[2] B. Webb and C.-F. Ma, Single-phase liquid jet impingement heat transfer, *Advances in Heat Transfer* (Elsevier, Amsterdam, 1995), Vol. 26, pp. 105–217.

[3] H. Fujimoto, W. Obana, M. Ashida, T. Hama, and H. Takuda, Hydrodynamics and heat transfer characteristics of oil-in-water emulsion droplets impinging on hot stainless steel foil, Exp. Therm. Fluid Sci. **85**, 201 (2017).

[4] M. Singh, H. M. Haverinen, P. Dhagat, and G. E. Jabbour, Inkjet printing process and its applications, Adv. Mater. **22**, 673 (2010).

[5] D. N. Papachristou and R. Barters, Resection of the liver with a water jet, Br. J. Surg. **69**, 93 (1982).

[6] T. Ohki, A. Nakagawa, T. Hirano, T. Hashimoto, V. Menezes, H. Jokura, H. Uenohara, Y. Sato, T. Saito, R. Shirane *et al.*, Experimental application of pulsed Ho:YAG laser-induced liquid jet as a novel rigid neuroendoscopic dissection device, Lasers Surg. Med. **34**, 227 (2004).

[7] Y. Tagawa, N. Oudalov, A. El Ghalbzouri, C. Sun, and D. Lohse, Needle-free injection into skin and soft matter with highly focused microjets, Lab on a Chip **13**, 1357 (2013).

[8] R. Reitz and F. Bracco, Mechanism of atomization of a liquid jet, Phys. Fluids **25**, 1730 (1982).

[9] H.-Y. Kim, Z. Feng, and J.-H. Chun, Instability of a liquid jet emerging from a droplet upon collision with a solid surface, Phys. Fluids **12**, 531 (2000).

[10] A. L. Yarin, Drop impact dynamics: Splashing, spreading, receding, bouncing, Annu. Rev. Fluid Mech. **38**, 159 (2006).

[11] L. Rayleigh, On the capillary phenomena of jets, Proc. R. Soc. London **29**, 71 (1879).

[12] E. Goedde and M. Yuen, Experiments on liquid jet instability, J. Fluid Mech. **40**, 495 (1970).

[13] J. Eggers and E. Villermaux, Physics of liquid jets, Rep. Prog. Phys. **71**, 036601 (2008).

[14] M. Rein, Phenomena of liquid drop impact on solid and liquid surfaces, Fluid Dyn. Res. **12**, 61 (1993).

[15] C. Josserand and S. T. Thoroddsen, Drop impact on a solid surface, Annu. Rev. Fluid Mech. **48**, 365 (2016).

[16] A. Vailati, L. Zinnato, and R. Cerbino, How archer fish achieve a powerful impact: Hydrodynamic instability of a pulsed jet in toxotes jaculatrix, PLoS One **7**, e47867 (2012).

[17] P. Coullet, L. Mahadevan, and C. Riera, Hydrodynamical models for the chaotic dripping faucet, J. Fluid Mech. **526**, 1 (2005).

[18] W. E. Ranz, *On Sprays and Spraying: A Survey of Spray Technology for Research and Development Engineers* (The Pennsylvania State University, Pennsylvania, 1956), Vol. 65.

[19] S. Lin and R. Reitz, Drop and spray formation from a liquid jet, Annu. Rev. Fluid Mech. **30**, 85 (1998).

[20] W. van Hoeve, S. Gekle, J. H. Snoeijer, M. Versluis, M. P. Brenner, and D. Lohse, Breakup of diminutive rayleigh jets, Phys. Fluids **22**, 122003 (2010).

[21] C. Clanet and J. C. Lasheras, Transition from dripping to jetting, J. Fluid Mech. **383**, 307 (1999).

[22] S.-P. Lin, *Breakup of Liquid Sheets and Jets* (Cambridge University Press, Cambridge, 2003).

[23] S. Leroux, C. Dumouchel, and M. Ledoux, The stability curve of newtonian liquid jets, Atom. Sprays **6**, 623 (1996).

[24] S. Leroux, C. Dumouchel, and M. Ledoux, The break-up length of laminar cylindrical liquid jets: Modification of weber's theory, Int. J. Fluid Mech. Res. **24**, 428 (1997).

[25] T. Kasyap, D. Sivakumar, and B. Raghunandan, Flow and breakup characteristics of elliptical liquid jets, Int. J. Multiphase Flow **35**, 8 (2009).

[26] A. Umemura, S. Kawanabe, S. Suzuki, and J. Osaka, Two-valued breakup length of a water jet issuing from a finite-length nozzle under normal gravity, Phys. Rev. E **84**, 036309 (2011).

[27] F. García, H. González, J. Castrejón-Pita, and A. Castrejón-Pita, The breakup length of harmonically stimulated capillary jets, Appl. Phys. Lett. **105**, 094104 (2014).

[28] A. M. Sterling and C. Sleicher, The instability of capillary jets, J. Fluid Mech. **68**, 477 (1975).

[29] C. Dumouchel, On the experimental investigation on primary atomization of liquid streams, Exp. Fluids **45**, 371 (2008).

[30] R. W. Fenn III and S. Middleman, Newtonian jet stability: the role of air resistance, AIChE J. **15**, 379 (1969).

[31] J. A. F. Plateau, *Statique Expérimentale et Théorique des Liquides Soumis aux Seules Forces Moléculaires* (Gauthier-Villars, Paris, 1873), Vol. 2.

[32] G. Amini and A. Dolatabadi, Capillary instability of elliptic liquid jets, Phys. Fluids **23**, 084109 (2011).

[33] G. Amini, Y. Lv, A. Dolatabadi, and M. Ihme, Instability of elliptic liquid jets: Temporal linear stability theory and experimental analysis, Phys. Fluids **26**, 114105 (2014).

[34] J. Eggers, Nonlinear dynamics and breakup of free-surface flows, Rev. Mod. Phys. **69**, 865 (1997).

[35] S. Leib and M. Goldstein, Convective and absolute instability of a viscous liquid jet, Phys. Fluids **29**, 952 (1986).

[36] J. B. Keller, S. Rubinow, and Y. Tu, Spatial instability of a jet, Phys. Fluids **16**, 2052 (1973).

[37] H. González and F. García, The measurement of growth rates in capillary jets, J. Fluid Mech. **619**, 179 (2009).

[38] H. González, P. A. Vazquez, F. J. García, and J. Guerrero, Minimal formulation of the linear spatial analysis of capillary jets: Validity of the two-mode approach, Phys. Rev. Fluids **3**, 044802 (2018).

[39] A. Ardekani, V. Sharma, and G. McKinley, Dynamics of bead formation, filament thinning and breakup in weakly viscoelastic jets, J. Fluid Mech. **665**, 46 (2010).

[40] J. Shinjo and A. Umemura, Simulation of liquid jet primary breakup: Dynamics of ligament and droplet formation, Int. J. Multiphase Flow **36**, 513 (2010).

[41] G. D. Martin, S. D. Hoath, and I. M. Hutchings, Inkjet printing-the physics of manipulating liquid jets and drops, J. Phys.: Conf. Ser. **105**, 012001 (2008).

[42] Y.-J. Chen and P. Steen, Dynamics of inviscid capillary breakup: collapse and pinchoff of a film bridge, J. Fluid Mech. **341**, 245 (1997).

[43] W. D. Wu, S. X. Lin, and X. D. Chen, Monodisperse droplet formation through a continuous jet break-up using glass nozzles operated with piezoelectric pulsation, AIChE J. **57**, 1386 (2011).

[44] D. Rutland and G. Jameson, A non-linear effect in the capillary instability of liquid jets, J. Fluid Mech. **46**, 267 (1971).

[45] P.-K. Wu, R. Miranda, and G. Faeth, Effects of initial flow conditions on primary breakup of nonturbulent and turbulent round liquid jets, Atom. Sprays **5**, 175 (1995).

[46] J. Gavis and M. Modan, Expansion and contraction of jets of newtonian liquids in air: Effect of tube length, Phys. Fluids **10**, 487 (1967).

[47] C. Weber, Zum zerfall eines flüssigkeitsstrahles, ZAMM-J. Appl. Math. Mech./Z. Angewand. Math. Mech. **11**, 136 (1931).

[48] M.-C. Yuen, Non-linear capillary instability of a liquid jet, J. Fluid Mech. **33**, 151 (1968).

[49] I. Frankel and D. Weihs, Stability of a capillary jet with linearly increasing axial velocity (with application to shaped charges), J. Fluid Mech. **155**, 289 (1985).

[50] B. Zhang, J. Li, P. Guo, and Q. Lv, Experimental studies on the effect of reynolds and weber numbers on the impact forces of low-speed droplets colliding with a solid surface, Exp. Fluids **58**, 125 (2017).

[51] Y. Yu and C. Hopkins, Experimental determination of forces applied by liquid water drops at high drop velocities impacting a glass plate with and without a shallow water layer using wavelet deconvolution, Exp. Fluids **59**, 1 (2018).

[52] L. Gordillo, T.-P. Sun, and X. Cheng, Dynamics of drop impact on solid surfaces: Evolution of impact force and self-similar spreading, J. Fluid Mech. **840**, 190 (2018).

[53] B. R. Mitchell, J. C. Klewicki, Y. P. Korkolis, and B. L. Kinsey, The transient force profile of low-speed droplet impact: measurements and model, J. Fluid Mech. **867**, 300 (2019).

[54] J. Philippi, P.-Y. Lagrée, and A. Antkowiak, Drop impact on a solid surface: short-time self-similarity, J. Fluid Mech. **795**, 96 (2016).

[55] D. Richard and D. Quéré, Bouncing water drops, Europhys. Lett. **50**, 769 (2000).

[56] A. M. Worthington, *A Study of Splashes* (Longmans, Green, and Co., England, 1908).

[57] D. A. Weiss and A. L. Yarin, Single drop impact onto liquid films: Neck distortion, jetting, tiny bubble entrainment, and crown formation, J. Fluid Mech. **385**, 229 (1999).

[58] N. Anantharamaiah, H. V. Tafreshi, and B. Pourdeyhimi, A study on hydroentangling waterjets and their impact forces, Exp. Fluids **41**, 103 (2006).

[59] See Supplemental Material at http://link.aps.org/supplemental/10.1103/PhysRevFluids.4.113603 for video of the normal impingement of Rayleigh jets (e.g., a steady-state jet, a wavy jet, and a droplet train).

[60] J. Li, B. Zhang, P. Guo, and Q. Lv, Impact force of a low speed water droplet colliding on a solid surface, J. Appl. Phys. **116**, 214903 (2014).